

"

S1. Description of the Ventersdorp imprints

The well preserved raindrop imprints used in this study (Fig. 1) are from Omdraaivlei farm near Prieska, South Africa, in the middle of the Kameeldoorns Formation (previously known as the Ongers River Arkose Formation) of the Platberg Group (formerly locally known as the Sodium Group) of the 2.7 Ga Ventersdorp Supergroup²⁵. The Ventersdorp Supergroup is widespread across the Kaapvaal Craton and is everywhere considered to be non-marine in depositional environment, attesting to a setting inboard within a continent. The raindrop-bearing sediments are underlain by fluvial conglomerates, and are overlain two formations above by stromatolitic carbonates, cherts and arkoses that have been interpreted as evaporative lacustrine facies²⁵. By comparison with modern equivalents, such rocks are most commonly deposited in continental interiors under semi-arid conditions. Our investigations identified several localities on at least 18 distinct bedding surfaces where raindrop imprints are exposed, spread over a distance of 3 km from a previously reported site²⁵. The imprints take the form of moderately to poorly overlapping rimmed craters ~1 mm deep and range from 0.7-11 mm in maximum dimension (Fig. 1a). The imprints penetrate into very poorly sorted (0.075 – 1.5 mm grain size with a weak mode around 0.25 mm) accretionary lapilli-vitric-crystal-lithic tuff of intermediate composition, and are draped by a 0.5 – 0.8 mm thick graded veneer of very fine-grained (<0.02 mm) volcanic ash (Fig. 1b and S1). The fine ash is relatively resistant to weathering, whereas the overlying ash has been extensively eroded away to leave imprinted surfaces protected by the fine ash veneer (a,c,

Fig. S1). Marginally curled mudflakes and desiccation cracks are developed on several raindrop horizons²⁵. As shown by slightly elliptical imprint outlines and mildly increased imprint density on the windward faces of underlying symmetrical wave-ripples (Fig. 1c), droplet acceleration by prevailing winds occurred but was insignificant. Close examination rules out gas bubble pits, water-drop pits formed by melting ice, hailstone imprints, micrometeorite or tektite impact craters, and accretionary or other lapilli impacts as responsible for the structures, as described in section S3.

S2. Paleo-elevation of the Ventersdorp imprints.

Although the exact paleo-elevation of the Ventersdorp imprints is unknowable, the error on the derived upper limit on pressure (or air density) will be less than ~10% assuming that the original elevation was less than a conservative 900 m. On the modern Earth, ~75% of land area is below 900 m elevation³², while in the Neoproterozoic (2.8-2.5 Ga), continental topography should have been generally lower because of a warmer, weaker lithosphere³³. A further constraint is found in the local geology (Fig. S2). The fining-upwards sediments of the Kameeldoorns Formation, within which the raindrop imprints are located, were deposited in a 460 m deep trough in the cratonized early Archaean basement at Omdraaivlei³⁴. Porphyritic lavas of the Makwassie Formation overtop the Kameeldoorns sediments, and elsewhere locally the Makwassie lavas cover the basement granite without further fluvial incision. This suggests that by the time the trough was filled by sediment, elevation approached the regional base-level. On cratons like the Kaapvaal on which the Ventersdorp Supergroup was deposited, base level is typically sea-level. Lastly, the 1.5 – 2 km thick underlying flood basalt

representing the Klipriviersberg Group that exists elsewhere in the Ventersdorp Supergroup is not present in the regional succession at Omdraaivlei, suggesting that the increase in elevation preceding or accompanying initial eruption of flood basalts³⁵ either did not occur locally or had subsided by the time of Kameeldoorns deposition.

S3. Elimination of alternative mechanisms for the formation of the Ventersdorp imprints

Other geological phenomena may produce structures similar to raindrop imprints. Among the alternatives are i) bubble-foam pits²⁶, ii) waterdrop pits formed by melting ice³⁶, iii) hailstone imprints¹⁴, iv) gas bubble pits³⁷⁻³⁹, v) lapilli impact craters, vi) micro-meteorite impact craters, vii) tektite impact craters or viii) secondary craters from other impacts.

Close field examination confirms that they are indeed raindrop imprints, as previously reported²⁵. The Ventersdorp imprints are unlikely to be bubble-foam pits or gas-bubble pits, because bubble pits typically have a circular morphology, while the Ventersdorp imprints are slightly elongated and show a mildly increased imprint density on the windward faces of underlying symmetrical wave-ripples (Fig. 1C). These observations strongly support an atmospheric source. Hailstone imprints tend to be deeper, often display internal melt rings⁴⁰ and bounce and roll marks would be expected. Waterdrop pits from melting ice are typically restricted to a small area, while the imprints in this study extend over several kilometers. Finally, craters formed by small solid impactors such as tektites, micro-meteorites or lapilli should be deeper, would leave

behind traces such as bounce-marks or roll-trails, or the impactors themselves would be preserved within or adjacent to the imprints. Such features were not observed.

S4. Ventersdorp Paleo-rainfall characteristics

The rain events that created the fossil imprints were likely light to moderate in intensity. Heavy rainfall (with large maximum drop sizes) leads to distorted imprints²⁶, which are not observed at Omdraaivlei. Furthermore, as imprints only occasionally overlap, this suggests rain showers of short duration. Because a thin layer of ash immediately covered the raindrop imprints following their formation (Fig. 1b and S1), it may be reasonable to assume that the rain events occurred between closely-spaced volcanic eruptions. The aqueous solubility of volcanic gases may have rendered the rain more acidic, but this would insignificantly affect the raindrop's physical properties, as discussed in Section S5-iv.

We assume that terminal velocity was reached for all raindrops that created the Ventersdorp imprints. Experiments with falling raindrops⁴¹ reveal that terminal velocity is reached in ~12 m. A vegetal canopy can prevent raindrops from falling at terminal velocity, but this concern does not apply here, as plants did not exist during the Archaean.

The largest possible raindrop size that created the biggest imprints was 6.8 mm. This corresponds to the largest drop ever measured at the surface²⁰ and a theoretical maximum from physics (from Eqs. 1 and 2 combined). To constrain how common such drops are in rain events, we can determine the probability that a heavy shower was

responsible for the raindrop imprints. The preservation of raindrop imprints is best attained in arid and semi-arid climates²⁶. The probability distribution functions (PDF) of rainfall rates for semi-arid climate zones^{42, 43} reveal that the probability of a rain event having a rainfall rate less than 100 mm hr⁻¹ ranges between 78% and 99% of all rain events.

Under the assumption that the raindrop size distributions associated with specific rainfall rates on the early Earth were similar to modern arid and semi-arid climates, such statistics favor an atmospheric density at 2.7 Ga that was lower than the present air density or, at most, comparable to it (Table S1). The imprint area histogram (Fig. S3b) reveals that the largest imprints (on which the upper limit on air density is based) represent 0.2% of the total number of imprints. The raindrop size distribution can be calculated for different rainfall rates from known analytical functions^{20, 44, 45}. In two well-characterized semi-arid sites, which are Niamey in Niger, and Dakar in Senegal, such relationships between the drop size distribution and rainfall rate have been derived empirically⁴⁵. Using these size distribution functions, the largest 0.2% of drops in rainfall events of 100 mm hr⁻¹ rate or greater have diameters that exceed 5.3 mm at Niamey and 5.1 mm at Dakar. We can also compare the raindrop diameter threshold for 0.2% of the raindrops by number at 100 mm hr⁻¹ rainfall rate using the drop size distribution function of Willis and Tattelman²⁰, which is a widely applied formulation in meteorology. This size distribution parameterization gives a limit of 3.8 mm for the largest 0.2% of the raindrops at 100 mm hr⁻¹ (Fig. S4). Lower rainfall rates generate a size distribution skewed towards smaller raindrops. Because rainfall rates less than 100 mm hr⁻¹ have a

much higher probability of occurrence in semi-arid areas, smaller raindrops are therefore more probable than the size threshold calculated at 100 mm hr^{-1} . Hence, the inferred air density from the 100 mm hr^{-1} rainfall rate is an upper limit.

On this basis, we define a “probable upper-limit zone” at raindrop diameters greater than 3.8 to 5.3 mm, and a “low probability zone” set conservatively at raindrop diameters $> 5.3 \text{ mm}$ because of uncertainty in Archaean raindrop size distribution. Given those dimensions, the corresponding air density upper-limit can be obtained from Fig. 4. Thus, assuming that rainfall rates and associated drop size distributions for modern semi-arid sites applied to similar climatic locations in the Archaean, the upper-limit of atmospheric density was between 0.6 and 1.3 kg m^{-3} , with 78-99% certainty.

S5. Methods

i) Measuring the Ventersdorp raindrop imprint dimensions. The largest Archaean imprints were measured in the field across their long and short axis to $\pm 0.5 \text{ mm}$ for later comparison with more precise laser-determined topography. Latex peels of the raindrops imprints were obtained by spreading low-viscosity latex on the imprints, letting the latex cure, and removing the peel. Many casts of the imprints were thus obtained recording 955 individual raindrop imprints. Latex peels were subsequently scanned using the G2 high-resolution three-dimensional laser scanner of Metron Corp. (Snoqualmie, WA). The vertical resolution of this instrument is $0.0002''$ (0.051 mm). Each scan line has a spacing of $0.002''$ (0.005 mm), and each data point from scan line l is offset a small amount in scan-line $l + 1$, resulting in a non-rectangular point-cloud of data. Each point-cloud was

then interpolated onto a rectangular grid using an inverse data-weighting (IDW) scheme to obtain a digital elevation model (DEM). Each DEM was then artificially “filled” (in the hydrological sense) in a Geographical Information System (GIS) software package, filling up imprints to their pour-point, which allowed computation of fill-volume and fill-surface area. Histograms of imprint area and volume (Fig. S4) were compiled, and the histogram bin-width was calculated using the method of Scott⁴⁶ as $bin\ width = 3.49\sigma N^{1/3}$ where σ is the standard deviation of the dataset and N the total number of measured imprints, with bin-width defining the error in measurement and constraining the number of bins in the histograms. As the latex peels were taken from draped surfaces (Section S1), the drape reduces the effective diameter of the measured imprints by $\sim 2\times$ the drape thickness. These results revealed a maximum imprint area of $A_{latex} = 50.30 \pm 0.625\text{ mm}^2$ and a volume of $V_{latex} = 16.71 \pm 0.73\text{ mm}^3$. Correcting for the ash drape thickness (0.5 mm) translates the area measurement to $A_{latex} = 63.6 \pm 0.7\text{ mm}^2$, which is consistent with the lower uncertainty of the average 5 largest imprint areas A_{insitu} measured in the field as $56 \pm 5.7\text{ mm}^2$, and corrected to $70 \pm 6.4\text{ mm}^2$.

ii) Experimental substrate physical characteristics. We used two sets of ash analogous to the Ventersdorp tuff as the substrate in our experimental investigation. The ash was placed and minimally compacted into 8” (20.3 cm) aluminium trays of 1” (2.5 cm) thickness. One “fresh” set of ash was only two months old from the 2010 Eyjafjallajökull eruption in Iceland, while the other was weathered late Pleistocene Pahala ash from Hawaii²⁸. Both ashes were from mafic to intermediate hydrovolcanic eruptions of a similar grain-size to ash hosting the Archaean raindrop imprints. The grain sizes of the

Eyjafjallajökull and Pahala ash were measured using a CAMSIZER® optical grain size analyzer from Retsch Technology (Fig. S5). The instrument measured the maximum and minimum diameter for each grain passing through the beam (many thousands were processed). The peak mode of the maximum diameter size distribution occurs at 0.48 mm and 0.21 mm for Eyjafjallajökull ash and Pahala ash respectively, while the peak mode of the minimum diameter size distribution occurs at 0.38 mm and 0.14 mm for Eyjafjallajökull ash and Pahala ash respectively. These dimensions compare well with those measured from the Ventersdorp tuff (Section S1). In addition, the silica content of the Eyjafjallajökull ash we used for the basis of our calculations is also similar to the Ventersdorp tuff (52% vs 58% for the Ventersdorp tuff, Table S2).

iii) Experimental substrate moisture content. In the original Ventersdorp raindrop imprints, all moisture was lost during the lithification process; as such the original moisture content of the ash present when the imprints formed is unknown. However, qualitative experimental observations showed little difference between 5 wt% and 10 wt% water, whereas 20 wt% water liquified the substrate such that imprints were not preserved. We chose 10% as a nominal moisture content. The observed difference in imprint dimensions is little provided that the substrate is “not too wet” (<20wt% water) so that it does not become a slurry. This was particularly true for crater area (the geometric measure we used to relate dimensionless momentum). Similar findings with raindrops of 3 mm in diameter obliquely impacting (at terminal velocity) muddy silt of different wetness also exhibit little change in crater area at intermediate moisture content⁴⁷. As such, we did not include uncertainties in moisture content in the calculation

of errors. The magnitude of this error is outweighed by the very conservative assumption of maximum raindrop size (Section S4), as raindrop size has a much larger control on imprint dimensions than does moisture content.

iv) Experimental droplet characteristics. Water droplets of different volumes (5, 10, 20, 50, 60, and 80 μl) were dropped indoors from a height of 27 m. Experimental droplet sizes were determined using a micro-pipette, allowing a drop-volume control of $\pm 1 \mu\text{l}$. Using this 1 μl -accurate pipette, we measured the mass of a dozen drops per drop size, and extrapolated a volume. The error bars in the x-dimension in Fig. 2 reflect the standard deviation of those measurements. We assumed that pure water (density = 1000 kg m^{-3}) droplets formed the imprints. Even acidic raindrops, akin to those falling near volcanoes today, would have essentially identical density. For example, the most extreme pH recorded within 2 km of the Kilauea crater⁴⁸ in Hawaii is 1.6, yet only a concentration of 850 ppm (0.085%) sulfuric acid (density = 1840 kg m^{-3}) is necessary to lower the pH of simulated rain⁴⁹ to 1.5. Such a low concentration insignificantly affects drop density. Droplet surface tension is also insignificantly affected by such low concentrations of sulfuric acid⁵⁰. Finally, if the raindrops were additionally ashy, a slightly different ash residue would have been expected in the bottoms of craters compared with the non-impacted surface, but no evidence of this was observed in thin section (Fig. S1).

v) Analysis of experimental substrate imprint dimensions. The experimental ash substrates with the newly formed imprints were “lithified” for further analyses. The uppermost millimeters of the substrate was first strengthened using approximately 10-15

coats of high-strength hair-spray, before low-viscosity liquid urethane plastic (Smooth-on Smooth-Cast 310) was slowly poured on, and absorbed by the porous substrate. Slightly excessive pours would leave low-viscosity liquid urethane plastic ponding at bottom of the imprints, which was removed using absorbent paper. After several hours of cure time, the result was a hardened (“fully lithified”) cratered substrate. The substrates were subsequently scanned with the same laser scanner used to measure the latex peels. The imprint dimensions were extracted from the topography using Geographical Information System (GIS) methods, and the calculated standard deviation forms the y-error bars in Fig. 2.

vi) Calculation of the theoretical relationship between air density and dimensionless momentum. We define dimensionless momentum as

$$J = \frac{V_{term} m_d}{\eta A_d} \quad \text{Eq. 3}$$

where V_{term} is the terminal velocity, m_d is the mass of the raindrop, η the dynamic viscosity (independent of ρ_{air}), and A_d the cross sectional area of the falling drop. We used a published method to calculate the theoretical relationship between the terminal velocity V_{term} of a drop of a particular size with air density¹⁸. Because the input is drop dimension, we directly calculate m_d and A_d , and thus J . We found it most convenient to generalize this relationship with the parametric representation:

$$\ln \rho_{air} = C_1 X^2 + C_2 X + C_3 \quad \text{Eq. S1}$$

where $X = \ln J$, as a quantitative relationship is quickly obtained given C_1 , C_2 and C_3 for different drop sizes. We provide Table S4 where C_1 , C_2 and C_3 coefficients are given for drops of different sizes.

vii) Calculation of experimental dimensionless momentum. For each droplet size, we measured a mean mass m , and a standard deviation σ_m based on weighing of a dozen droplets per size, from which we obtained a corresponding volumetric mean V and mass standard deviation σ_v by dividing by the density ρ .

The first step is to obtain the equivalent radius: $r_{eq} = \left(\frac{3V}{4\pi}\right)^{1/3}$ Eq. S2

and its error:

$$\delta r_{eq} = \left(\frac{\partial r_{eq}}{\partial V} \sigma_v\right) = \left(\frac{3}{4\pi}\right)^{1/3} \left(\frac{V^{-2/3}}{3}\right) \sigma_v \quad \text{Eq. S3}$$

Next, we obtain the cross-sectional area of the drop:

$$A_{eq} = \pi r_{eq}^2 \quad \text{Eq. S4}$$

and its error:

$$\delta A_{eq} = 2\pi r_{eq} (\delta r_{eq}) \quad \text{Eq. S5}$$

To calculate the terminal velocity, we use the equation of the Reynolds number Re and write

$$V_{term} = \frac{Re\eta}{2r_{eq}\rho_{air}}, \quad \text{Eq. S6}$$

where η is the dynamic viscosity (independent of air density) and ρ_{air} is air density, or expressed in terms of m :

$$V_{term} = \frac{Re\eta}{2\rho_{air}\left(\frac{3}{4\rho\pi}\right)^{\frac{1}{3}}} m^{\frac{1}{3}} \quad \text{Eq. S7}$$

The error is expressed as

$$\delta V_{term} = \left(\left(\left(\left(\frac{\partial V_{term}}{\partial m} \right) \sigma_m \right)^2 \right)^{\frac{1}{2}} = \frac{Re\eta}{6\rho_{air}\left(\frac{3}{4\rho\pi}\right)^{\frac{1}{3}}} m^{\frac{4}{3}} \sigma_m \quad \text{Eq. S8}$$

The Re value are obtained from the empirical relationships⁵¹ of Berry and Pranger (1974).

Finally, the uncertainty in dimensionless momentum is

$$\delta J = \left[\left(\frac{\partial J}{\partial V_{term}} \delta V_{term} \right)^2 + \left(\frac{\partial J}{\partial m} \sigma_m \right)^2 + \left(\frac{\partial J}{\partial A_{eq}} \delta A_{eq} \right)^2 \right]^{\frac{1}{2}}, \quad \text{Eq. S9}$$

or

$$\delta J = \left[\left(\frac{m}{\eta A_{eq}} \delta V_{term} \right)^2 + \left(\frac{V_{term}}{\eta A_{eq}} \sigma_m \right)^2 + \left(\frac{-V_{term} m}{\eta A_{eq}^2} \delta A_{eq} \right)^2 \right]^{\frac{1}{2}} \quad \text{Eq. S10}$$

which are the x-error bars in Fig. 2. Therefore, for each drop size, we can calculate dimensionless momentum and the corresponding error, and fit the curve with a second order polynomial. We naturally force the fit to cross the origin.

For compatibility with Eq. S1, and to have the x-axis be identical with Fig. 3b, we fitted the curve in log space:

$$\ln A = 0.1172 (\ln J)^2 - 1.3960 (\ln J) \quad r^2 = 0.97 \quad \text{Eq. S11}$$

However, we need $X = \ln J$ in order to solve for air density in Eq. S1, therefore we express $\ln J$ on the left hand side. If the fit is performed by switching the abscissa and the ordinate, we obtain:

$$\ln J = -1.0021 (\ln A)^2 + 7.6342 (\ln A) \quad r^2 = 0.89 \quad \text{Eq. S12}$$

The difference in r^2 comes from forcing the fit to go through the origin. As such, we use the first relationship (Eq. S11) rearranged for $\ln J$ because of the better fit :

$$\ln J = 5.9556 + 4.2662(1.9488 + 0.4688 \ln A)^{1/2} \quad \text{Eq. S13}$$

where A is in mm^2 .

viii) Calculation of air density. The dimensions of the raindrop imprints measured using the latex peels are consistent with the lower bound of measurements done in-situ. To calculate an atmospheric density upper-bound, we use the lower bound on the largest raindrop imprint area, because smaller imprint areas reflect lower raindrop terminal velocities and thus higher air density. That measurement, corrected for the ash drape thickness, is $A_{\text{latex}} - 1\sigma = 62.9 \text{ mm}^2$. This value is inserted into Eq. S13 to obtain $\ln J(X)$, which is then used in Eq. S1 yielding an air density, ρ_{air} of 2.3 kg m^{-3} . However, it is unknown what the actual maximum raindrop size was in the Archaean rainstorms. Fig. 4 illustrates the expected atmospheric density when the maximum raindrop size is varied. In addition, it is very probable that the maximum size of the raindrops that created the Ventersdorp imprints was between 3.8 and 5.3 mm equivalent diameter, a more typical maximum in storms, because the rainfall rates associated with the maximum recorded drop sizes of 6.8 mm are unusually rare, large and highly erosive²⁶ (Section S4). This yields a probable upper limit for atmospheric density of $< 0.6 - 1.3 \text{ kg m}^{-3}$, and an absolute upper-limit of $< 2.3 \text{ kg m}^{-3}$.

32. Gurnis, M. Bounds on global dynamic topography from Phanerozoic flooding of continental platforms. *Nature* **344**, 754-756 (1990).
33. Rey, P. F. & Coltice, N. Neoproterozoic lithospheric strengthening and the coupling of Earth's geochemical reservoirs, *Geology* **36**, 635-638 (2008).
34. Van der Westhuizen, W. & de Bruijn, H. High temperature ash flow-wet

- sediment interaction in the Makwassie Formation, Ventersdorp Supergroup, South Africa. *Precambrian Res.* **101**, 341-351 (2000)
35. Campbell, I.H. Large Igneous Provinces and the Mantle Plume Hypothesis. *Elements* **1**, 265-269 (2005).
36. Reineck H. Abschmelzrate von Treibeis an den Ufersäumen des Gezeiten-Meeress. *Senckenbergiana lethaea* **37**, 299 – 304 (1956).
37. Maxson, J.H. Gas pits in non-marine sediments. *J. Sediment. Petrol.* **10**, 142-145 (1940).
38. Cloud, P.E. Gas as a sedimentary and diagenetic agent. *Am. J. Sci.* **258**, 35-45. (1960)
39. Rindsberg, A. K. Gas-escape structures and their paleoenvironmental significance at the Steven C. Minkin Paleozoic footprint site (Early Pennsylvanian, Alabama). In: Buta, R.; Rindsberg A. & Kopaska-Merkel, D. (Ed.), *PENNSYLVANIAN FOOTPRINTS IN THE BLACK WARRIOR BASIN OF ALABAMA*. Alabama Paleontological Society Monograph No, 1 (2005).
40. Rubin, D. & Hunter, R. Sedimentary structures formed in sand by surface tension on melting hailstones. *J. Sed. Res.* **54**, 581-582 (1984)
41. Gunn, R. & Kinzer, G. The terminal velocity of fall for water droplets in stagnant air. *J. Atm. Sci.* **6** : 243-248 (1949).
42. Lebel, T., Taupin, J.D., & D'Amato, N. Rainfall monitoring during the HAPEX-Sahel. 1. General rainfall conditions and climatology. *J. Hydrol.* **188-189**, 74-96 (1997).
43. Sauvageot, H. The probability density function of rain rate and the estimation of

- rainfall by area integrals. *J. Appl. Meteorol.* **33**, 1255-1262 (1994)
44. Marshall, J.S. & Palmer, W. McK. The distribution of raindrops with size. *J. Meteorol.* **5**, 165-166 (1948).
 45. Ochou, A.B., Nzeukou, A., & Sauvageot, H. Parametrization of drop size distribution with rain rate. *Atmos. Res.* **84**, 58-66 (2007).
 46. Scott, D. On optimal and data-based histograms. *Biometrika* **66**, 605-610 (1979).
 47. Hladil, J. & Berousek, P. Oblique raindrop impacts. *Bull. Geosci.* **68**, 23-32 (1993).
 48. Nachbar-Hapai, M. *et al.* Acid Rain in the Kilauea Volcano Area (Hawaii). *Arch. Environ. Contam. Toxicol.* **18**, 65-73 (1989).
 49. Ferenbaugh, R. Effects of simulated acid rain on *Phaseolus Vulgaris* L. (Fabacea). *Amer. J. Bot.* **63**, 283-288 (1976).
 50. Suggitt, R. M., Aziz, P. M. & Wetmore, F.E.W. Surface tension of sulfuric acid. *J. Am. Chem. Soc.* **71**, 676-678 (1949).
 51. Berry, E.X. & Pranger, M.R. Equations for calculating the terminal velocity of water drops. *J. Appl. Meteorol.* **13**, 108-113 (1974).

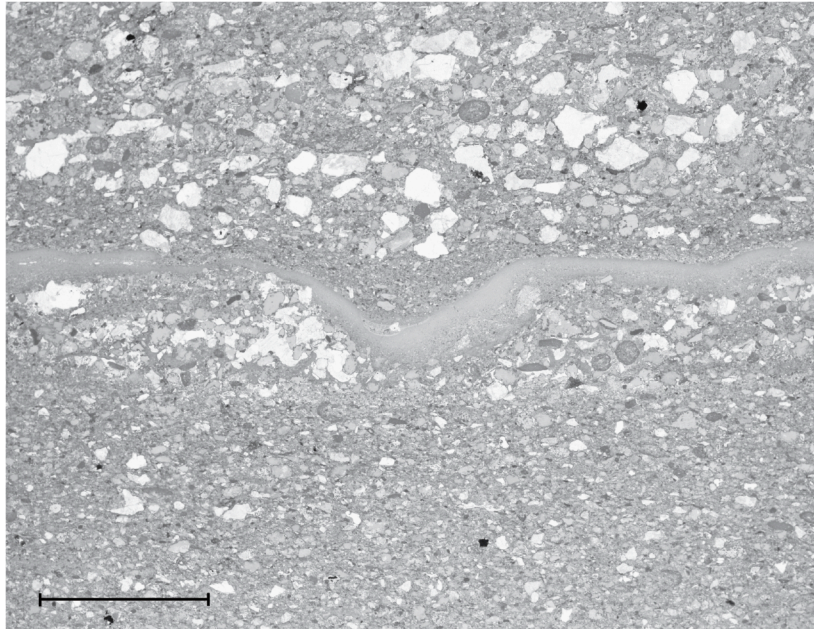


Figure S1: Thin section of the rock slab from Fig. 1b. The imprints penetrate 1-2 mm into poorly-sorted coarse (0.075 – 1.5 mm grain size with a weak mode around 0.25 mm) accretionary lapilli-vitric-crystal-lithic tuff, and are draped with a thin veneer (~0.5 mm) of very fine-grained (<0.02 mm) volcanic ash. The coarse ash above the drape has been weathered away at many sites, revealing the preserved raindrop imprints on draped bedding planes in the field. Scale bar is 5 mm. (Photo credit: Thomas Tobin).

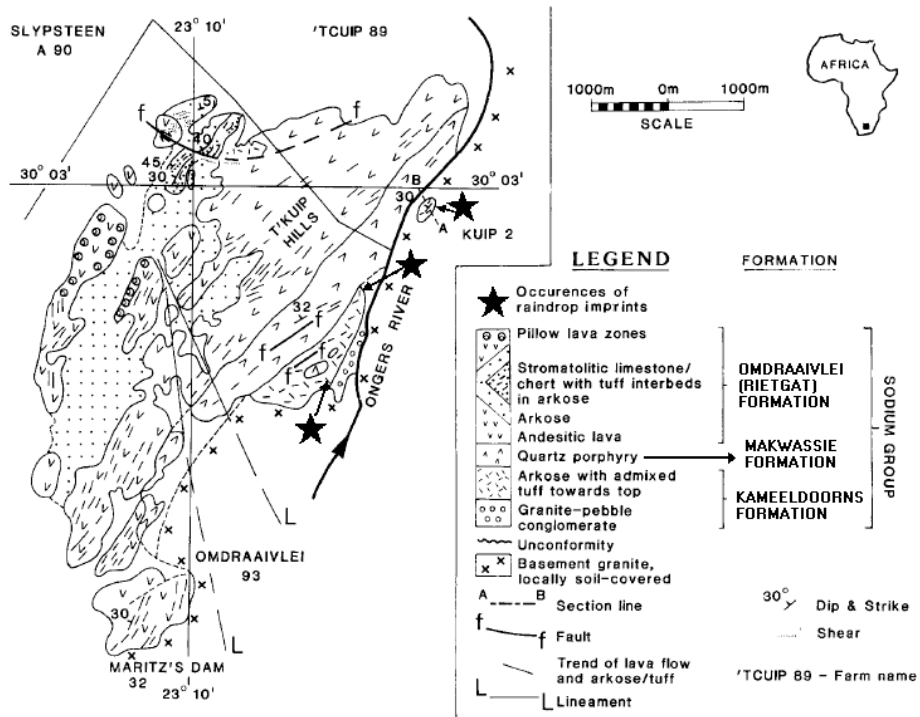


Figure S2. Local geology surrounding the Omdraavlei raindrop imprint site²⁵.

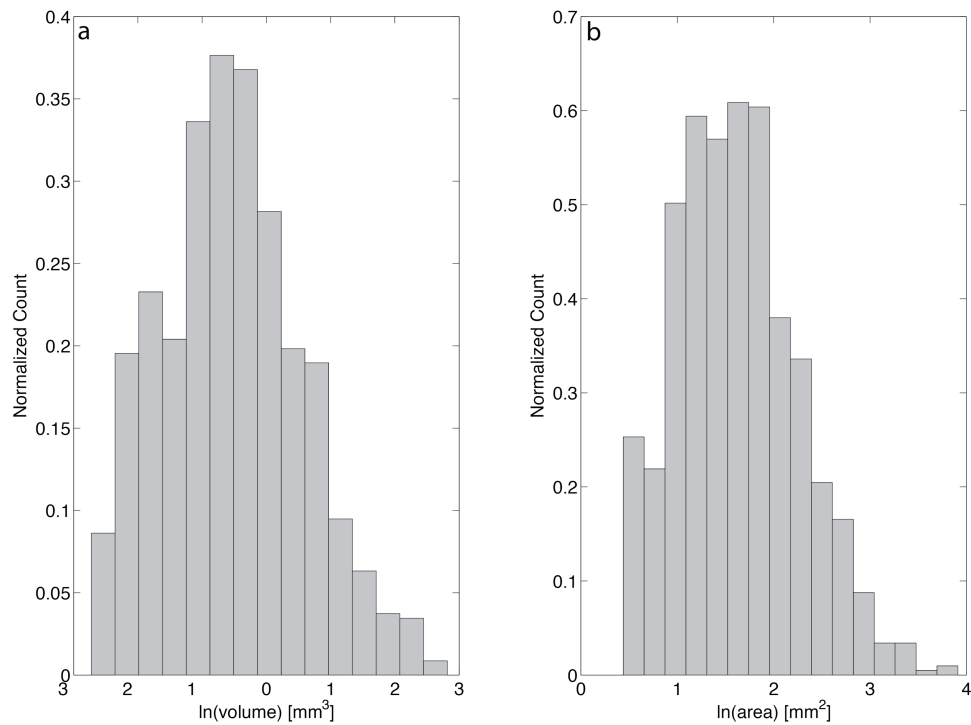


Figure S3: Histograms of the 955 imprints measured from latex peels. a) imprint volume, b) imprint area. The bin width for each histogram was calculated using the method of Scott⁴¹ (Supplementary Information). The rightmost bin in each histogram identifies the largest imprint volume and area respectively. They are not necessarily correlated with the same physical imprint. The bin width is the measurement error.

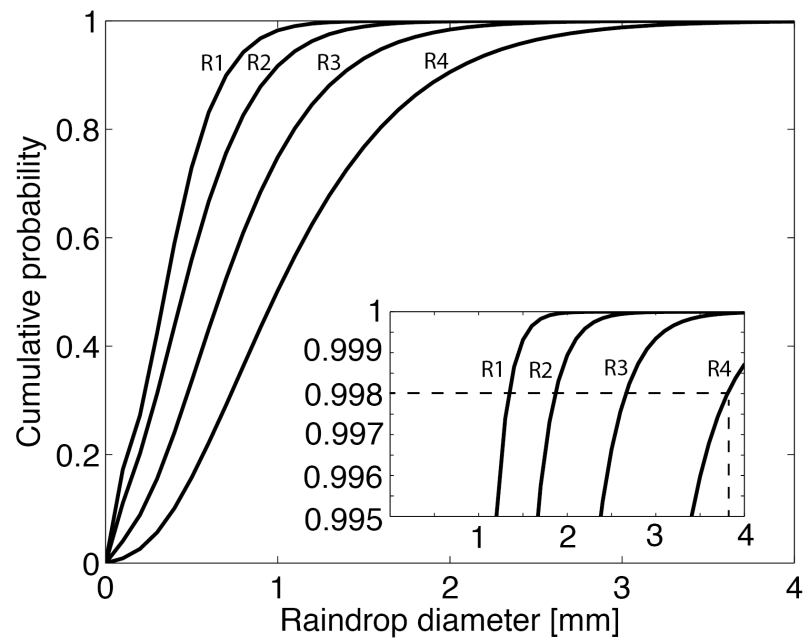


Figure S4. Modern raindrop cumulative size distribution function according to Willis and Tattelman²⁰. Rainfall rates are R1 = 0.1 mm hr⁻¹, R2 = 1 mm hr⁻¹, R3 = 10 mm hr⁻¹, and R4 = 100 mm hr⁻¹. Inset represents the same data enlarged to reveal the tail of the distributions, showing that the largest 0.2% of raindrops are >3.8 mm in diameter for rainfall rate R4.

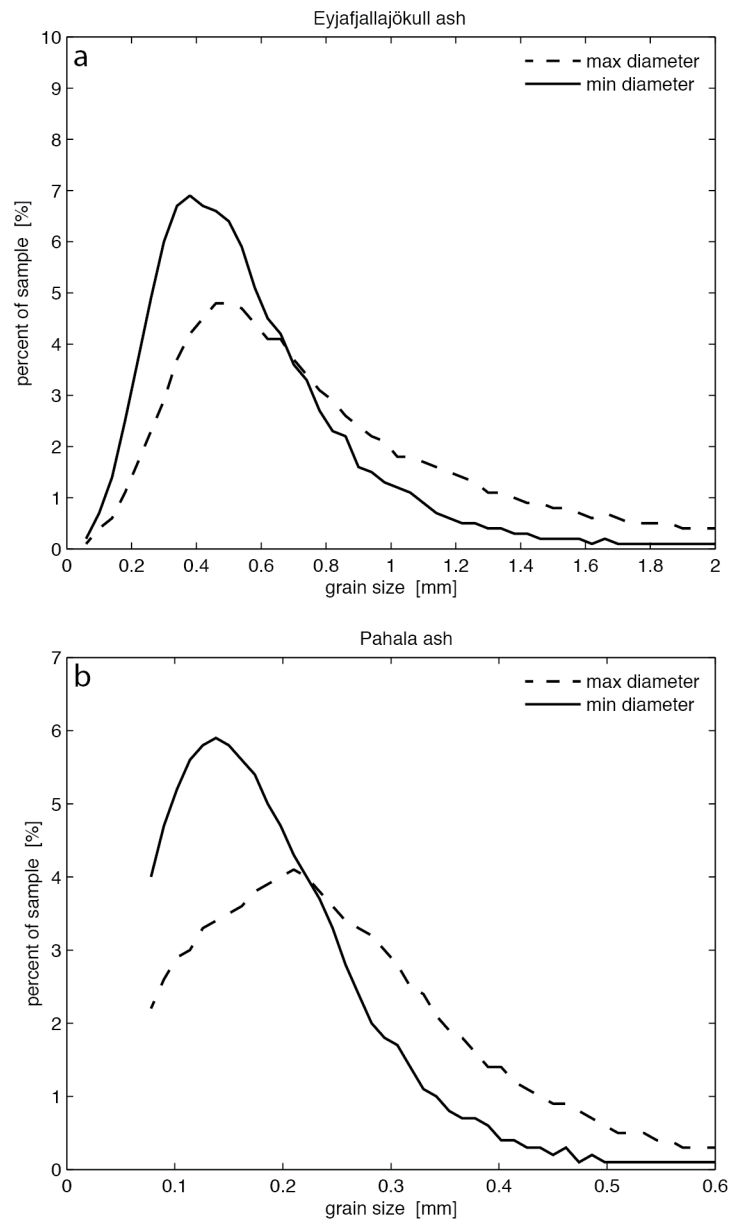


Figure S5: Grain size analysis of the ash used as substrate in the experimental investigation. a) Eyjafjallajökull ash; b) Pahala ash.

Table S1: Dimension threshold for 0.2% of raindrop diameters obtained using different raindrop size distribution parameterizations at a rainfall rate of 100 mm hr⁻¹. The air density corresponding to the raindrop diameter threshold is determined from Fig. 4 and is an upper limit, given that rainfall rates are more likely to be less than 100 mm hr⁻¹ in semi-arid locations.

| Reference for raindrop size distribution function | raindrop diameter threshold at 0.2% by number of the drop size distribution | Corresponding Archaean air density constraint |
|---|---|---|
| Willis and Tattelman ²⁰ | 3.8 mm | ≤0.6 kg m ⁻³ |
| Marshall and Palmer ⁴⁴ | 4.0 mm | ≤0.7 kg m ⁻³ |
| Ochou et al. ⁴⁵ (Dakar) | 5.1 mm | ≤1.2 kg m ⁻³ |
| Ochou et al. ⁴⁵ (Niamey) | 5.3 mm | ≤1.3 kg m ⁻³ |

Table S2: Major element composition of the experimental ash substrates and Ventersdorp tuff obtained by X-ray Fluorescence, and normalized on a volatile-free basis with total Fe expressed as FeO. LOI is “Loss on Ignition:”

| Major Elements | Eyjafjallajökull ash (Normalized weight %) | Pahala ash (Normalized weight %) | Ventersdorp tuff (Normalized weight %) |
|--------------------------------|--|--|--|
| SiO ₂ | 58.49 | 46.56 | 52.02 |
| TiO ₂ | 1.479 | 2.322 | 1.766 |
| Al ₂ O ₃ | 14.88 | 12.09 | 15.46 |
| FeO | 8.76 | 13.60 | 13.61 |
| MnO | 0.208 | 0.241 | 0.186 |
| MgO | 3.48 | 16.00 | 7.28 |
| CaO | 5.09 | 6.07 | 6.38 |
| Na ₂ O | 5.29 | 2.38 | 2.78 |
| K ₂ O | 2.05 | 0.44 | 0.27 |
| P ₂ O ₅ | 0.266 | 0.291 | 0.247 |
| Total | 100.00 | 100.00 | 100.00 |
| LOI (%) | -0.25 | 8.00 | 7.97 |
| Cl ≥ | 0.12 | 0.44 | 0.01 |

Table S3: Trace element composition of the experimental ash substrates and Ventersdorp tuff obtained by X-ray Fluorescence.

| Trace elements | Eyjafjallajökull ash (Unnormalized [ppm]) | Pahala ash (Unnormalized [ppm]) | Ventersdorp tuff (Unnormalized [ppm]) |
|----------------|---|---------------------------------------|---|
| Ni | 69 | 680 | 111 |
| Cr | 101 | 920 | 216 |
| Sc | 15 | 28 | 33 |
| V | 105 | 203 | 233 |
| Ba | 440 | 106 | 505 |
| Rb | 45 | 7 | 6 |
| Sr | 282 | 211 | 82 |
| Zr | 552 | 117 | 138 |
| Y | 67 | 20 | 37 |
| Nb | 65.7 | 11.9 | 7.3 |
| Ga | 28 | 17 | 19 |
| Cu | 31 | 73 | 342 |
| Zn | 155 | 122 | 181 |
| Pb | 5 | 2 | 55 |
| La | 56 | 9 | 13 |
| Ce | 118 | 29 | 27 |
| Th | 5 | 0 | 1 |
| Nd | 59 | 15 | 16 |
| U | 2 | 1 | 0 |
| Sum tr. | 2201 | 2572 | 2021 |
| In % | 0.22 | 0.26 | 0.20 |

Table S4: Constants used in Eq. 4 to determine air density from dimensionless momentum for falling drops of different diameter d .

| | | | |
|--|--|--|--|
| $d = 1 \text{ mm}$ | $d = 2 \text{ mm}$ | $d = 3 \text{ mm}$ | $d = 4 \text{ mm}$ |
| $C_1 = -0.1558$ $C_2 = +1.0500$ $C_3 = +9.5627$ | $C_1 = -0.1241$ $C_2 = +0.8696$ $C_3 = +9.9444$ | $C_1 = -0.0900$ $C_2 = +0.2520$ $C_3 = +13.5852$ | $C_1 = -0.0695$ $C_2 = -0.1765$ $C_3 = +16.4312$ |
| $d = 5 \text{ mm}$ | $d = 6 \text{ mm}$ | $d = 6.8 \text{ mm}$ | $d = 7 \text{ mm}$ |
| $C_1 = -0.0570$ $C_2 = -0.4533$ $C_3 = +18.4177$ | $C_1 = -0.0475$ $C_2 = -0.6755$ $C_3 = +20.0701$ | $C_1 = -0.0413$ $C_2 = -0.8262$ $C_3 = +21.2326$ | $C_1 = -0.0406$ $C_2 = -0.8408$ $C_3 = +21.3530$ |